Catalysis Today 462 (2026) 115574

Contents lists available at ScienceDirect

Catalysis Today

journal homepage: www.elsevier.com/locate/cattod

Enhancing CO_2 hydrogenation via spatially engineered bifunctional catalysts: Toward selective $C_{8–10}$ aromatics for sustainable aviation fuel

Hyeonji Yeom, Yongseok Kim, Hanbit Jang, Jongmin Park, Seongeun Kim, Kyungsu Na *

Department of Chemistry, Chonnam National University, 77 Yongbong-ro, Buk-gu, Gwangju 61186, Republic of Korea

ARTICLE INFO

Keywords:
CO_2 hydrogenation
Spinel oxide
Nanosheet zeolite
Catalyst proximity
Alkylated benzene
Sustainable aviation fuel

ABSTRACT

The direct CO_2 hydrogenation into liquid-phase hydrocarbons offers a sustainable route for carbon recycling, yet achieving high selectivity toward sustainable aviation fuel-range aromatic compounds remains challenging. Here, we report a bifunctional catalyst system composed of FeK-loaded $CuAl_2O_4$-based catalyst (FeK/CAO) and a nanosheet MFI-type zeolite (NS-HMFI) with hierarchical porosity for the selective production of $C_{8–10}$ aromatic hydrocarbons. Structural and compositional characterizations confirmed the mesoporous architecture and strong acidity of NS-HMFI and the multifunctional activity of FeK/CAO in CO_2 activation and C–C coupling. By engineering the spatial proximity between the two catalysts through four integration methods such as physical mixture (PM), granule mixture (GM), dual-bed system (DB), and multi-bed system (MB), we elucidated the relationship between proximity and catalytic performance. Among the systems tested, the GM system achieved the highest CO_2 conversion (39.2 %) with the lowest CO selectivity (13.0 %) due to enhanced CO_2 adsorption and dissociation facilitated by potassium migration and increased surface basicity. Conversely, the DB system, with minimal catalyst proximity, promoted the highest aromatic distribution and enabled selective conversion of light olefins into $C_{8–10}$ aromatics. All systems integrating NS-HMFI showed >95 % distribution for $C_{8–10}$ aromatics among total aromatics, highlighting the critical role of external acid sites in mesoporous zeolites. This work demonstrates a proximity-controlled catalytic approach for efficient CO_2 hydrogenation to SAF-range aromatics and provides mechanistic insights into the design of multifunctional hybrid catalysts.

1. Introduction

The catalytic hydrogenation of CO_2 into value-added hydrocarbons presents a compelling solution for reducing greenhouse gas emissions and enabling a circular carbon economy [1–3]. As the world moves towards a circular carbon economy, CO_2 utilization technologies have emerged as promising solutions for reducing atmospheric CO_2 levels while simultaneously producing value-added chemicals. Among these, the catalytic hydrogenation of CO_2 into liquid hydrocarbons holds great potential as a sustainable alternative to conventional fuels, contributing to the decarbonization of various industrial sectors. In recent years, extensive research has focused on development of novel catalysts [3–5], optimization of reaction conditions [6,7], and elucidation of structure–activity relationships for various catalytic materials [7–9]. Among various catalysts investigated, a $CuAl_2O_4$ (denoted as CAO) spinel oxide has demonstrated remarkable activity in reverse water–gas shift (RWGS) reaction with high CO_2 conversion, making it ideal candidate for CO_2 hydrogenation process [10]. Notably, the incorporation of alkali and transition metals, constructing K-promoted Fe-supported CAO structure (i.e., FeK/$CuAl_2O_4$, denoted as FeK/CAO), has exhibited significantly enhanced CO_2 hydrogenation efficiency, attributed to synergistic effects between the active phases and improved H_2 activation [11–14]. In these bifunctional catalytic systems, heat treatment of $CuAl_2O_4$ affects its structural properties and the extent of hydrogen spillover, which in turn influences product selectivity, promoting the formation of either olefins or paraffins depending on the specific structural characteristics [14].

In CO_2 hydrogenation, beyond high catalytic activity, controlling product selectivity is also an important challenge. Depending on the target application such as chemicals or fuels, selective formation of olefins, paraffins, alcohols, or aromatics must be achieved. Such selectivity can be finely tuned by adjusting catalyst composition [15,16], structure [8,17–19], type of metal [20,21], metal–support interaction [9,22], presence of promoters or inhibitors [23,24], and reaction conditions such as temperature, pressure, and CO_2/H_2 ratio. To produce longer-chain hydrocarbons and aromatics, zeolites have been integrated as secondary catalytic components in bifunctional systems. Their

* Corresponding author.
E-mail address: kyungsu_na@chonnam.ac.kr (K. Na).

https://doi.org/10.1016/j.cattod.2025.115574
Received 15 July 2025; Received in revised form 2 September 2025; Accepted 19 September 2025
Available online 23 September 2025

inherent strong acidic property, micropore size/shape selectivity, and robust crystalline framework facilitate transformations such as oligomerization, aromatization, and isomerization [25–27]. This integration between metal-based catalysts and zeolites plays a pivotal role in determining product selectivity. More specifically, after the main catalyst initiates the activation of CO_2 and H_2 followed by C–C chain growth, the acid catalytic sites of zeolite could activate hydrocarbon species and thereby change the final product selectivity. Wei et al. demonstrated the effectiveness of a highly efficient multifunctional catalyst, which consisted of a Na-Fe_3O_4 combined with H-ZSM-5 zeolite (Na-Fe_3O_4/H-ZSM-5), for the direct conversion of CO_2 into gasoline-range hydrocarbons [27]. Furthermore, Noreen et al. introduced a triple-bed system consisting of a NaFe catalyst, followed by SAPO-11 and ZSM-5 zeolites, which effectively maximized the selectivity for iso paraffins [28].

The catalyst bed type can significantly influence catalytic performance by affecting the interaction between the metal catalyst and zeolite, as well as the efficiency of reactant diffusion. Several bed systems are commonly used in catalytic processes: powder mixture (PM), granule mixture (GM), dual-bed (DB), and multi-bed (MB) systems. In powder mixture, the metal catalyst and zeolite are finely ground and thoroughly blended, promoting intimate contact between the phases [29,30]. While this approach can enhance catalytic activity, it may lead to issues with mass transfer and rapid deactivation [31]. Granule mixture improves stability by allowing better diffusion pathways for reactants while maintaining intimate contact between the catalytic phases [32]. However, powder and granule mixture has traditionally been less favored due to concerns about the migration of alkali metals, which could lead to zeolite deactivation over time [33]. In contrast, dual-bed and multi-bed systems physically separate the metal oxide-based catalyst and zeolite catalyst, helping to mitigate the risk of alkali migration [27,34]. While this separation helps maintain the integrity of the zeolite, dual-bed systems often face limitations in efficiency and space-time yields due to less effective mass transfer between the phases [35].

In this study, we employed various types of integration methods combining FeK/CAO with a nanosheet zeolites. This nanosheet zeolite with short b-axis 2D structure provides structural advantages over bulk zeolites in terms of enhancing mass transport and utilizing abundant external acid sites [36–38]. These structural differences facilitate more efficient alkylation reactions, which are critical for producing larger hydrocarbons, resulting in a notable increase in alkylated C_{8-10} aromatic molecules. Importantly, the increase of C_{8-10} aromatics distribution aligned with the growing demand for sustainable aviation fuel (SAF) which gained traction as a promising low-carbon alternative to conventional jet fuel. A crucial attribute of high-quality SAF is its controlled aromatic contents up to 25 %. These aromatic contents contribute to essential fuel properties such as energy density, combustion characteristics, and elastomer compatibility (seal swelling) [39] and are largely composed of C_{8-10} aromatics. In summary, our study demonstrates the potential of FeK/$CuAl_2O_4$ catalysts integrated with nanosheet zeolite. By carefully controlling the zeolite integration, and mixing strategy, we achieved high yields of C_{8-10} aromatic compounds that are main component of SAF aromatics [39].

2. Experimental section

2.1. Materials preparation

2.1.1. Synthesis of CAO

The synthesis of CAO was conducted using a co-precipitation method. In a typical procedure, 0.06 mol (12.255 g) of aluminum isopropoxide (>98 %, Sigma Aldrich) was dissolved in 80.0 g of isopropyl alcohol in a round-bottomed flask. The resulting solution was then heated on a hot plate under reflux and stirring at 80 °C for 2 h. Subsequently, 10.0 mL of an aqueous solution of $Cu(NO_3)_2{\cdot}2.5\ H_2O$ (0.03 mol, 6.977 g, 98 %, Sigma Aldrich) was added dropwise to the flask, followed by further heating under reflux and stirring at 80 °C for 3 h. Upon cooling to room temperature, the solution was titrated with 1 M KOH solution (Daejung Chemicals & Metals) to adjust the pH to 9.5. The resulting solution was stirred for an additional 3 h, resulting in the formation of a solid precipitate. The precipitate was filtered and subsequently dried in an oven at 100 °C for 12 h. The obtained dried powder was further subjected to calcination in a furnace at temperatures of 800 °C for 4 h under an air flow (100 mL min^{-1}) to yield crystalline CAO.

2.1.2. Synthesis of FeK/CAO

The K-promoted Fe catalysts supported on CAO were prepared via a wet impregnation method utilizing CAO as the support material. Specifically, 1.0 g of CAO was suspended in 100.0 mL of deionized water within a round-bottomed glass flask. Subsequently, the desired quantities of $Fe(NO_3)_3{\cdot}9H_2O$ (≥98 %, Sigma Aldrich) and KNO_3 (99 %, Daejung Chemicals & Metals) were added to the solution, and the mixtures were stirred for 1 h at room temperature (25 °C). Following evaporation of the excess water at 70 °C, the mixtures were dried in an oven at 100 °C overnight. The resulting solid was then subjected to calcination in a furnace at 550 °C for 4 h under an air flow (100 mL min^{-1}) to yield a FeK/CAO.

2.1.3. Preparation of $C_{22-6-6}Br_2$ surfactant

The $C_{22-6-6}Br_2$ surfactant was synthesized via a reported procedure [36,37]. The detailed procedure was as follows: 51.7 g (0.3 mol) of N,N,N',N'-tetramethyl-1,6-diaminohexane (> 98.0 %, TCI) and 11.7 g (0.03 mol) of 1-bromodocosane (> 98.0 %, TCI) were dissolved in 400 mL acetonitrile/toluene mixture (1:1 v/v) and magnetically stirred at 60 °C for 12 h. The solvent was removed using a rotary evaporator at 45 °C (120 rpm). To the residual solution, 400 mL of diethyl ether (Daejung Chemicals & Metals) was added, followed by cooling in a refrigerator. The precipitated product was filtered, washed with diethyl ether, and dried in a vacuum oven at 50 °C. 14.0 g (0.025 mol) of the product and 8.4 g (0.05 mol) of 1-bromohexane (98 %, Sigma Aldrich) were dissolved in 300 mL acetonitrile and refluxed for 10 h. After cooling in a refrigerator, the product was filtered, washed with diethyl ether, and dried in a vacuum oven at 50 °C.

2.1.4. Synthesis of NS-HMFI

The NS-HMFI zeolite materials were synthesized using the quaternary ammonium surfactant (denoted as $C_{22-6-6}Br_2$) as the hierarchically unilamellar structure directing agent via a reported method [36,37]. In a typical synthesis of NS-HMFI zeolites, water glass (29 wt% aqueous solution, Si/Na = 1.57, Daejung Chemicals & Metals), sodium aluminate (41 wt% Na_2O, 53 wt% Al_2O_3, Na/Al = 1.27, Sigma Aldrich), H_2SO_4 (98 %, Daejung Chemicals & Metals), $C_{22-6-6}Br_2$, and distilled water were used to obtain a gel composition of Al_2O_3:33 Na_2O:100 SiO_2:7.5 $C_{22-6-6}Br_2$:24 H_2SO_4:4000 H_2O for Si/Al= 50. First, the water glass solution was added to the surfactant solution at once under vigorous magnetic stirring at room temperature. To this solution, an aqueous solution of sodium aluminate was added dropwise under vigorous stirring. Thereafter, an aqueous solution of H_2SO_4 was rapidly added to this solution. The resultant mixture was immediately shaken by hand or with a mechanical stirrer very vigorously for 5 min to obtain a homogeneous gel. After further stirring for 6 h with a magnetic stirrer in an oven at 60 °C, the gel mixture was transferred to a Teflon-lined stainless steel autoclave and heated at 150 °C for 4 days with a rotation of 60 rpm. The products were filtered and washed with distilled water and then dried in an oven at 130 °C, followed by calcined at 550 °C for 4 h under air flow. Finally, to convert the Na-form to the H-form, the calcined zeolites were ion-exchanged with 1 M NH_4NO_3 aqueous solution, and then the product was calcined at 550 °C for 4 h.

2.2. Material characterization

The metal loadings of Fe and K present in the series of FeK/CAOs were determined using inductively coupled plasma–optical emission spectroscopy (ICP–OES). The ICP–OES were performed utilizing an Avio 550 Max instrument (PerkinElmer). X-ray diffraction (XRD) patterns were acquired using a Rigaku MiniFlex 600 apparatus equipped with Cu Kα radiation (λ = 0.1541 nm) at 600 W (40 kV, 15 mA). All measurements were conducted under ambient conditions with a step size of 0.005 °, a scanning rate of 1 ° min^{-1}, and a 2θ range spanning from 15 to 80 °. Scanning electron microscopy (SEM) images were captured using Gemini 500 (ZEISS, 3 kV) in the absence of metal coating. Transmission electron microscopy (TEM) images were obtained using a JEM-2100F instrument (JEOL Ltd.) operating at 200 kV. The elemental composition was determined by energy dispersive spectroscopy (EDS) (X-Max 80 T, Oxford Instruments plc, UK). CO_2 or NH_3 temperature-programmed desorption (TPD) measurements were performed using the BEL-CAT analyzer (BEL, Osaka, Japan) with a mass spectrometer (MS) detector. Prior to measurements, samples were reduced under a 5 % H_2/Ar stream for 2 h at 400 °C in a quartz cell, followed by cooling to 50 °C with helium purge to remove residual H_2. CO_2 or NH_3 adsorption occurred using CO_2 or NH_3 flow over 1 h. After purging the cell with helium for 30 min, the TPD-MS process involved increasing the temperature from 50 to 1000 °C at a rate of 10 °C min^{-1} under helium flow. CO pre-absorbed H_2 temperature-programmed surface reaction (TPSR) was performed using the same BEL-CAT analyzer with a mass spectrometer (MS) detector. Prior to measurements, samples were reduced under a 80 % H_2/Ar stream for 2 h at 400 °C in a quartz cell, followed by cooling to 50 °C with Ar purge to remove residual H_2. CO adsorption occurred using a 10 % CO/He flow over 1 h. After purging the cell with Ar for 30 min, the TPSR-MS process involved increasing the temperature from 50 to 800 °C at a rate of 10 °C min^{-1} under 80 % H_2/Ar flow.

2.3. Reaction study

The catalytic reaction was conducted in a continuous flow fixed-bed microreactor with an inner diameter of 10.0 mm, which was equipped with a thermocouple positioned at the center of the catalyst bed. The catalyst, ranging from 0.5 g of FeK/CAO and consisting of 40−60 mesh particles, underwent reduction at 400 °C for 4 h under a flow of H_2 (60 mL min^{-1}) and Ar (50 mL min^{-1}), with a gas hourly space velocity (GHSV) of 10,000 mL g_{cat}^{-1} h^{-1}. For the powder mixture (PM), granule mixture (GM), dual-bed (DB), and multi-bed (MB) systems, 0.5 g FeK/CAO was mixed with 0.5 g nanosheet H^+-MFI (NS-HMFI) to form catalyst bed. The GHSV for these systems was 5000 mL g_{cat}^{-1} h^{-1}. Subsequently, a gas mixture comprising CO_2, H_2, and Ar (in a volumetric ratio of 21:63:16) was introduced into the reactor, pressurizing it to 3.0 MPa, with Ar serving as an internal standard gas. The reaction was conducted at 320 °C. The effluent gases were analyzed using a gas chromatograph (GC, YL6500, YOUNG IN Chromass, Korea) equipped with both a thermal conductivity detector (TCD) and a flame ionization detector (FID). These detectors were connected to a packed column (Supelco Analytical Metal packed GC column for TCD) and a capillary column (GS-GasPro for FID). Liquid products were collected using a cold trap (−4 °C) and subsequently manually injected into the GC using a micro syringe. The liquid products were analyzed with an FID connected to a capillary column (DB-5).

CO_2 conversion, and CO selectivity were determined on a molar carbon basis. The hydrocarbon distribution was computed using the total carbon moles, expressed in units of C-mol%, across all tested catalysts:

$$CO_2\ conversion(\%) = \frac{CO_{2,in} - CO_{2,out}}{CO_{2,in}} \times 100\%$$

where $CO_{2,in}$ and $CO_{2,out}$ denote the moles of CO_2 fed to the reactor and exhausted from the reactor after the reaction, respectively.

$$CO\ selectivity(\%) = \frac{CO_{out}}{CO_{2,in} - CO_{2,out}} \times 100\%$$

where CO_{out} represents the moles of CO produced during the reaction and exhausted from the reactor.

The distribution of individual hydrocarbons (C_i) in total hydrocarbons was given according to

$$C_i\ hydrocarbon\ distribution\ (C-mol\%) = \frac{mol\ of\ C_i\ hydrocarbon \times i}{\sum_{i=1}^{n} mol\ of\ C_i\ hydrocarbon \times i} \times 100\%$$

The carbon balances for all the reactions were approximately 95 %.

The catalytic activity was expressed as site time yield (STY) of aromatics according to

$$STY\ (g_{CH}\ kg_{cat}^{-1}\ h^{-1}) = \frac{GHSV_{CO_2} \times m \times Conv. \times S_{Aro.}}{W \times 22400}$$

where $GHSV_{CO2}$ is GHSV of CO_2 reflecting volumetric ratio, m is the molecular weight of CH (13 mol^{-1}), $Conv.$ represents the CO_2 conversion, $S_{Aro.}$ represents the selectivity of aromatics including CO, and W represents the mass of FeK/CAO and zeolite catalysts.

3. Results and discussion

3.1. Physicochemical properties of FeK/CAO and NS-HMFI

Fig. 1a shows the XRD pattern of fresh FeK/CAO catalyst, wherein distinct XRD reflections indicate the presence of crystalline phases of $CuAl_2O_4$, CuO, and Fe_2O_3. The crystalline spinel structure of $CuAl_2O_4$ occupied the major phase with lower concentrations of CuO and Fe_2O_3. The FeK/CAO shows a type-IV N_2 adsorption isotherm, indicating that the FeK/CAO consisted of mesoporous framework (Fig. 1b and Table S1). The BET surface area, the total pore volume and the average pore diameter of FeK/CAO were calculated as 48 m^2 g^{-1}, 0.20 cm^3 g^{-1} and 16.4 nm (Table S1). The SEM and TEM images of FeK/CAO show that the FeK/CAO was constructed in the form of nanoparticles that are aggregated with the formation of interparticle mesopores (Fig. 1c–d). The content of Fe and K was determined by ICP–OES to be 22 and 5 wt%, respectively (Table S1), which is close to the optimized composition that exhibited the best catalytic performance for achieving a high productivity of C_{5+} liquid-phase hydrocarbon [11,14].

Fig. 2a shows the XRD pattern of NS-HMFI zeolite, wherein the broad XRD reflections were observed with marked peaks that could be indexed as (*h0l*) planes. The broad XRD patterns indicate that the NS-HMFI zeolite consisted of tiny zeolite crystals, and the marked (*h0l*) peaks indicate that the zeolite crystals in NS-HMFI were formed as thin nanosheet structure with wide (*a*–*c*) planes along *b*-axis (Fig. 2a). The N_2 adsorption isotherm of NS-HMFI zeolite showed steep increase of adsorption volume at low relative pressure ($P/P_0 < 0.1$) and steady increase of adsorption volume at the P/P_0 ranges of 0.5–0.9 with type IV-pattern, indicating the presence of hierarchically microporous and mesoporous structure (Fig. 2b and Table S1). The BET surface area, the total pore volume and the average pore diameter of NS-HMFI were calculated as 670 m^2 g^{-1}, 1.31 cm^3 g^{-1} and 7.8 nm (Table S1). The SEM and TEM images in Fig. 2c–d also demonstrated the thin nanosheet morphology with intersheet mesopores. The actual Si/Al ratio was determined by ICP–OES to be 50 (Table S1). The mesoporosity of NS-HMFI could enhance mass transfer, providing facile access to acid sites of the zeolite, which was expected to effectively induce the synergy of metal-acid catalysis with FeK/CAO.

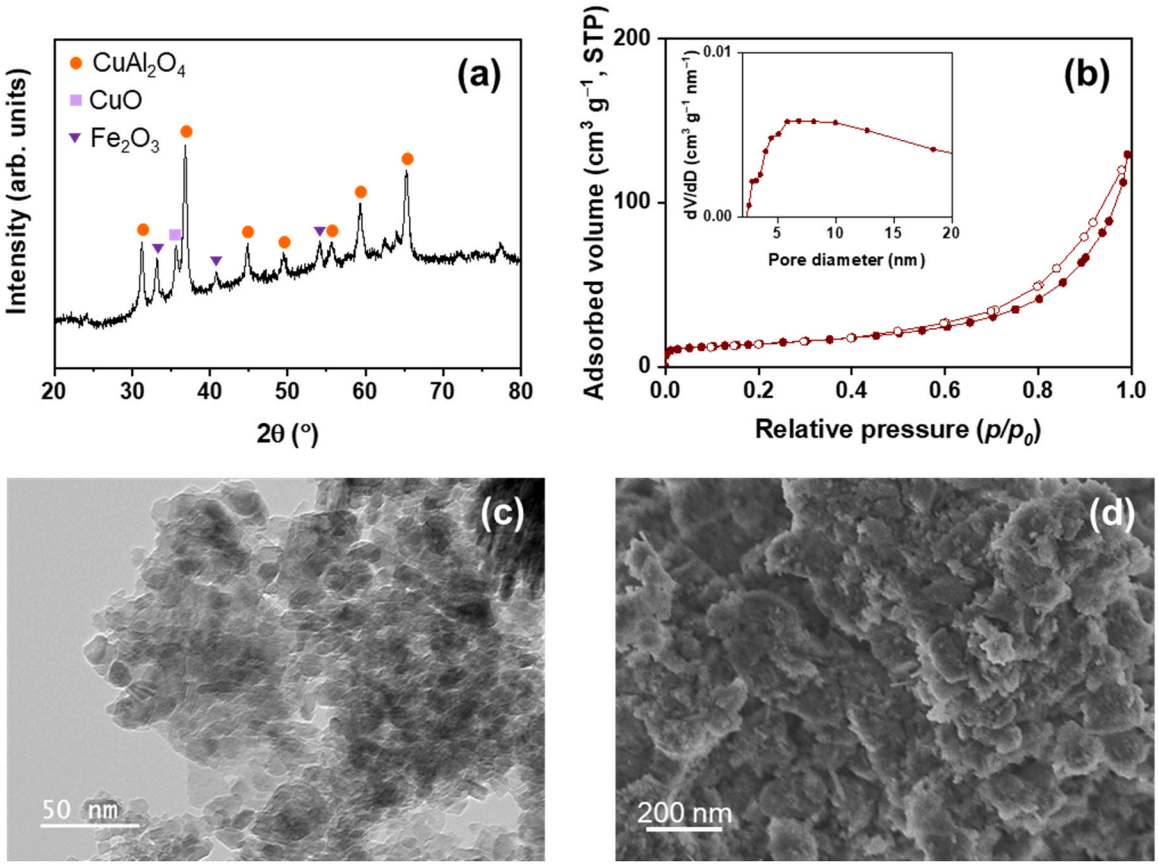

Fig. 1. (a) XRD pattern of fresh FeK/CAO catalyst. (b) N_2 adsorption isotherm of FeK/CAO catalyst and its corresponding pore size distributions (inset) derived from the adsorption branch using the BJH algorithm. (c) TEM image and (d) SEM image of the FeK/CAO catalyst.

3.2. Effect of proximity between FeK/CAO and NS-HMFI on CO_2 hydrogenation

As the basis of catalytic performance, the sole catalytic activity of FeK/CAO was investigated in the CO_2 hydrogenation. The FeK/CAO exhibited CO_2 conversion of 32.6 % with CO selectivity of 25.3 % (Fig. 3a and Table 1). Among the hydrocarbon distribution excluding CO, aliphatic C_{5+} hydrocarbons were produced as the major product with 49.1 % distribution (Table 1). It is noteworthy that the low-molecular weight olefins (i.e., C_{2-4}^{o}) were produced with almost four times higher distribution than paraffins (i.e., C_{2-4}^{p}), resulting in the highest C_{2-4} o/p ratio of 3.98 (Table 1). The product distribution revealed that the FeK/CAO actively played catalytic roles for RWGS reaction, C–C coupling reaction, and hydrogenation. Aromatic products were also produced, but its distribution was negligible with below 1 % and was not significant compared to other reactions. These catalytic functions were likely associated with the intrinsic amphoteric properties of FeK/CAO, which could facilitate CO_2 adsorption and activation, as well as carbon chain growth via C–C coupling (Fig. S1a–b and Table S2) [27]. Furthermore, when FeK/CAO catalyst was integrated with NS-HMFI, which has negligible CO_2 adsorption capacity (Fig. S1c and Table S2), the acidity of the zeolite could promote secondary transformations such as oligomerization, aromatization, and hydrogenation of hydrocarbon intermediates (Fig. S1d and Table S2). These complementary properties might alter the hydrocarbon distribution.

Because of the intrinsic catalytic activity of zeolite due to its acidic framework, it has been reported that the presence of zeolite could shift the reaction equilibrium and the mechanistic pathway of main catalyst for CO_2 hydrogenation [27,40−43]. To investigate the effect of zeolite addition to FeK/CAO, we controlled the proximity of FeK/CAO and zeolite in the composite catalysts by controlling the integration methods. Four different integration methods to build four different reaction environments have been investigated in this work (Fig. 3b): (i) physical mixture (PM) of two different catalysts as the powder form, (ii) granule mixture (GM) of two different catalysts prepared as the 40–60 mesh particles, (iii) dual-bed (DB) system of two different catalysts prepared as the 40–60 mesh particles that are separated by quartz wool, and (iv) multi-bed (MB) system of two different catalysts prepared as the 40–60 mesh particles (Fig. 3b).

The series of different catalyst integrations could control the proximity of two major catalysts, i.e., FeK/CAO and NS-HMFI. The proximity between FeK/CAO and NS-HMFI is the highest in PM system, in which two different catalysts in the powder form were mixed with the highest homogeneity as confirmed by the photograph of PM composite catalyst (Fig. 3b). The PM system could be considered as one catalytic reaction system consisting of FeK/CAO and NS-HMFI that operate mutually during the CO_2 hydrogenation. In contrast, in the GM system, two different catalysts prepared as the 40–60 mesh particles were mixed heterogeneously with lower proximity as confirmed by the photograph of GM composite catalyst wherein dark brown FeK/CAO particles and white zeolite particles were clearly distinguished (Fig. 3b). In this case, two different catalyst systems could be spatially distanced more than PM system, but their catalytic functions could exert mutual influence on each other. In the DB system, NS-HMFI and FeK/CAO prepared as the 40–60 mesh particles were respectively in the bottom and top layers that were separated by quartz wool to prevent direct contact between two catalysts (Fig. 3b). Two different catalyst systems were spatially separated at a considerable distance, such that their catalytic functions could operate independently with minimal mutual influence, expecting the cascade catalytic plays of FeK/CAO initially and NS-HMFI later. Consequently, the proximity between FeK/CAO and NS-HMFI decreased with the order of PM, GM and DB. In the MB system, FeK/CAO was in the

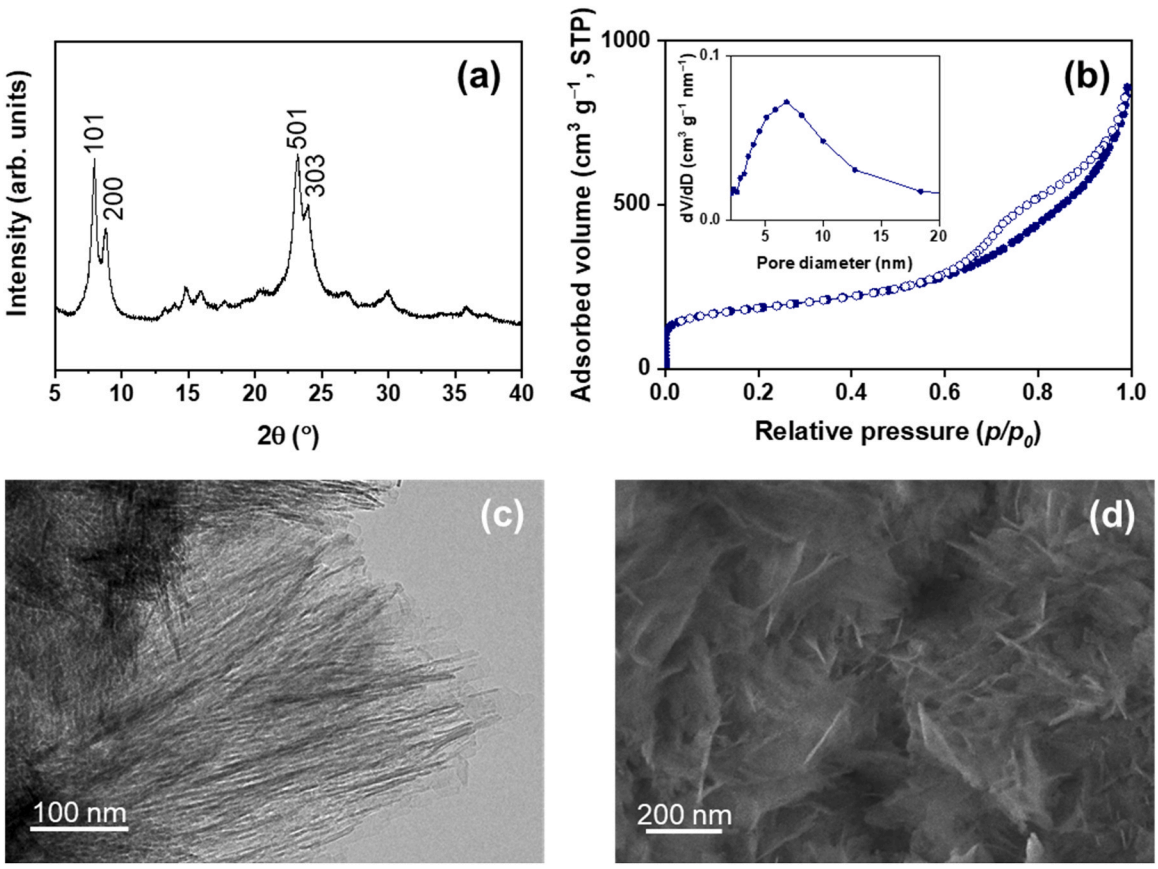

Fig. 2. (a) XRD pattern of fresh NS-HMFI zeolite displaying vertical *hkl* lines. (b) N_2 adsorption isotherm of NS-HMFI zeolite and its corresponding pore size distributions (inset) derived from the adsorption branch using the BJH algorithm. (c) TEM image and (d) SEM image of the NS-HMFI zeolite.

first and third catalyst layers, and NS-HMFI was in the second and fourth catalyst layers from top to bottom, wherein all catalyst layers were separated by quartz wool to prevent direct contact between different catalysts (Fig. 3b). In the case of MB system, the one-cycle cascade reaction that could occur on DB system could repeat twice.

The reaction results were summarized in Fig. 3a and Table 1, which were averaged from the 48 h of reaction profiles given in Fig. 4. Compared to the sole play of the FeK/CAO catalyst, when the NS-HMFI zeolite was integrated regardless of integration methods, the distribution for aromatics increased significantly accompanying with the decreases in C_{2-4} o/p ratio. It implies that the NS-HMFI zeolite played a crucial role for formation of aromatic products. However, there are appreciable differences in reaction results depending on the catalyst integration methods. The PM system showed a marginal decrease in CO_2 conversion and CO selectivity, with a remarkable increase in aromatics distribution compared to FeK/CAO catalyst. Despite CO selectivity decreased, CO_2 conversion decreased simultaneously, which could be attributed to the acid-base trade-off between zeolite and FeK/CAO due to the closest proximity between two catalysts in PM system. Therefore, the PM system constructed by physical mixture of powder-form of FeK/CAO and NS-HMFI would not be beneficial for enhancement of CO_2 hydrogenation. Meanwhile, distribution for low-molecular weight paraffins increased contrary to the decrease in olefins distribution, resulting in the C_{2-4} o/p ratio of 1.06. The decrease of C_{2-4} light olefins could be attributed to either hydrogenation of pre-formed C_{2-4} light olefins to C_{2-4} light paraffins or conversion of pre-formed C_{2-4} light olefins to aromatics. The increase in aromatics distribution was induced by the well-known olefin to aromatization pathways contributed by an acid catalytic play of zeolites with microporous framework affording size/shape-selective catalytic reactions [44–47].

In the case of GM system, the NS-HMFI and FeK/CAO catalysts prepared as the 40–60 mesh particles were distributed with farther distance than in the PM system. The resultant GM system is expected to construct inter-granule macropores that enhance efficiency of molecular diffusion. The two catalysts were still in a close proximity enabling synergistic sequential catalytic plays of FeK/CAO-based CO_2 activation and NS-HMFI zeolite-based acid-catalytic transformation of intermediate species supplied from FeK/CAO. The GM system achieved the highest CO_2 conversion of 39.2 % and the lowest CO selectivity of 13.0 %, showing significantly improved catalytic performance compared to other catalysts. Furthermore, compared to other catalyst system, the GM system showed a relatively more sustainable catalytic performance without significant changes in CO_2 conversion and hydrocarbon distribution (Fig. 4b). Both GM and PM system were constructed with FeK/CAO and NS-HMFI zeolite, but the spatial arrangement of the two phases led to distinct product distribution. In the PM system, the olefins generated on FeK/CAO were able to rapidly diffuse to the closely located zeolite domains, thereby increasing the probability of secondary transformation into aromatics and paraffins. In contrast, in the GM system, the larger inter-granule spacing placed the catalyst farther apart, which limited the contact between olefins and zeolites. As a result, a fraction of the olefins escaped without further transformation, leading to a higher proportion of untransformed olefins and lower distribution toward both aromatics and paraffins compared with the PM system. Despite the lower distribution of aromatics and C_{2-4}^{P} compared with the PM system, the close proximity between FeK/CAO and NS-HMFI zeolite with inter-granule macropores would enhance CO_2 hydrogenation with minimized CO selectivity. FeK/CAO would initiate CO_2 conversion to CO, that could be further converted to hydrocarbons. Subsequently, formation of aromatic products would be accelerated on the zeolite catalyst by consuming the C_{2-4} light olefins formed from FeK/CAO, which quickly shift the reaction equilibrium on FeK/CAO toward

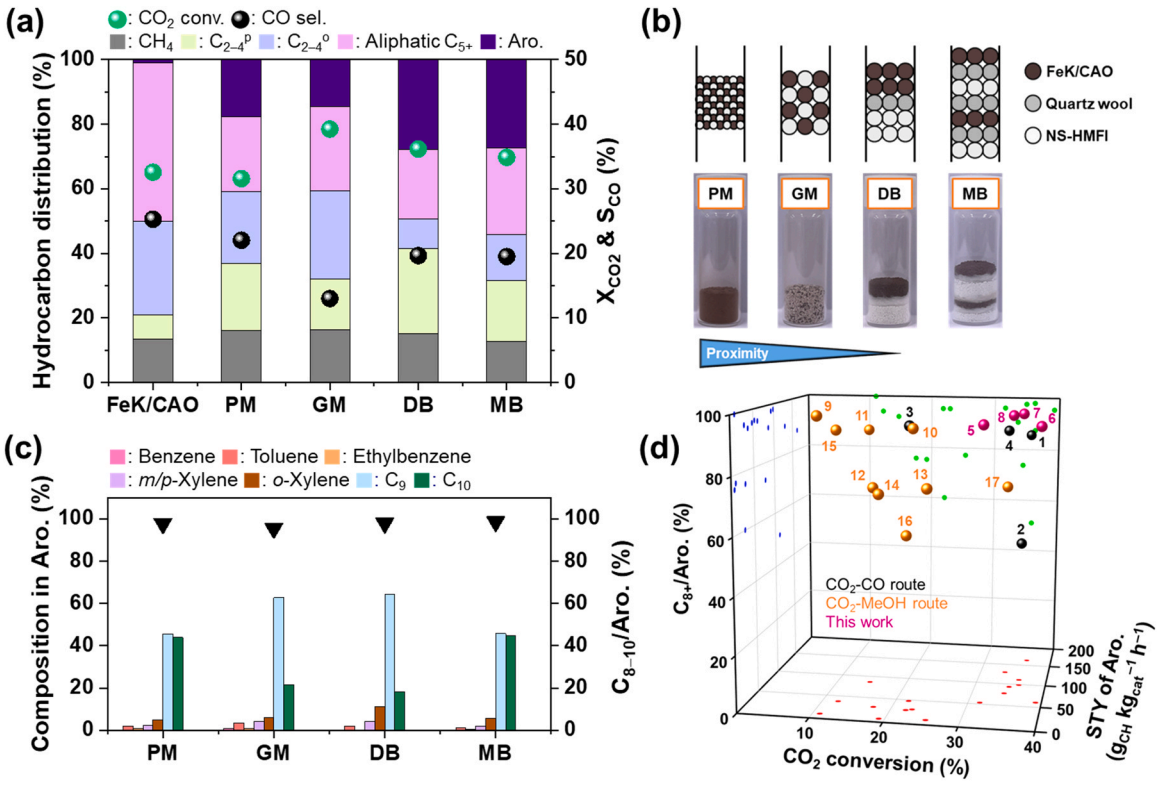

Fig. 3. (a) Averaged catalytic performances obtained from the CO_2 hydrogenation for 48 h (shown in Fig. 4) using FeK/CAO catalyst and NS-HMFI zeolite with different integration methods of powder mixture (PM), granule mixture (GM), dual-bed (DB), and multi-bed (MB), and (b) the schematized representation showing the four different integration methods and their actual photos. In (a), 0.5 g of the FeK/CAO catalyst was used alone, or a mixture of 0.5 g FeK/CAO catalyst and 0.5 g of NS-HMFI zeolite was integrated in four different methods (Reaction conditions: $T = 320$ °C, $P = 3.0$ MPa, $H_2/CO_2 = 3$, GHSV = 10,000 mL g_{cat}^{-1} h^{-1} for FeK/CAO, 5000 mL g_{cat}^{-1} h^{-1} for PM, GM, DB, and MB, respectively). (c) Composition in aromatic compounds determined by GC-MS, represented in (a) with percentage of C_{8-10} aromatic compounds in all aromatics (inverse triangle with black color). (d) Comparison of catalyst performance in CO_2 hydrogenation with the results reported elsewhere: the numbers shown in (d) correspond to the numbers in Table S4.

Table 1
Summary of the performances of the FeK/CAO with different integration manners.

Catalyst	GHSV (mL g_{cat}^{-1} h^{-1})	X_{CO2}[a] (%)	S_{CO}[b] (%)	Hydrocarbon distribution (%)					o/p ratio[c]
				CH_4	C_{2-4}^p	C_{2-4}^o	Aliphatic C_{5+}	Aromatics	
FeK/CAO	10,000	32.6	25.3	13.5	7.3	29.1	49.1	0.9	3.98
Physical mixture (PM)	5 000	31.6	22.0	16.2	20.8	22.1	23.2	17.7	1.06
Granule mixture (GM)		39.2	13.0	16.2	15.8	27.3	26.1	14.5	1.73
Dual-bed (DB)		36.2	19.7	15.0	26.4	9.1	21.6	27.9	0.35
Multi-bed (MB)		34.9	19.5	12.8	18.7	14.3	27.0	27.2	0.76

[a] CO_2 conversion
[b] CO selectivity
[c] olefin/paraffin ratio in C_{2-4} hydrocarbons

CO_2 consuming forward reaction. The inter-granule macropores contributed to faster diffusion of reactant, intermediate and product molecules. As a consequence, the GM system could exhibit the highest CO_2 conversion with the lowest CO selectivity. The catalytic role of NS-HMFI zeolite became more evident in the DB system. When FeK/CAO was in the top layer, fresh reactant mixture of CO_2 and H_2 was activated firstly via well-known CO_2 hydrogenation reaction pathways including RWGS, C–C coupling, and hydrogenation, which might construct a product distribution observed by sole catalytic play of FeK/CAO (Fig. 3a and Table 1). The products then should be diffused to the bottom layer filled with NS-HMFI zeolite. Compared to the other catalyst system, the DB system showed the highest aromatics distribution and the lowest C_{2-4} o/p ratio of 0.35 (see reaction results for FeK/CAO and DB in Fig. 3a and Table 1). It clearly proposes that the NS-HMFI zeolite would produce aromatic hydrocarbons by converting C_{2-4} light olefins produced independently from FeK/CAO spatially separated on the top layer, reminiscent of olefin to aromatics [40,43,48]. More specifically, benzene would be produced when three ethylene molecules assembled, and trimethylbenzene isomers would be produced when three propylene molecules assembled in various ways (Scheme 1). Such contribution on formation of aromatic molecules was observed in all the catalyst system integrated with NS-HMFI zeolite, implying that the formation of aromatic molecules is deeply involved with the presence of NS-HMFI zeolite (Fig. 3a and Table 1).

We further analyzed the aromatic molecules to reveal the specific aromatic components as summarized in Table 2. Among the aromatic molecules, we focused more carefully on the C_{8-10} aromatic molecules that are generally selected as the suitable aromatic compounds satisfying the requirement for using in SAF blend [49]. Relatively more volatile aromatic molecules such as benzene and toluene could not meet the requirements as the aromatic compounds in SAF, but alkylated C_{8-10} aromatic molecules could satisfy the requirements [49]. Therefore, it is

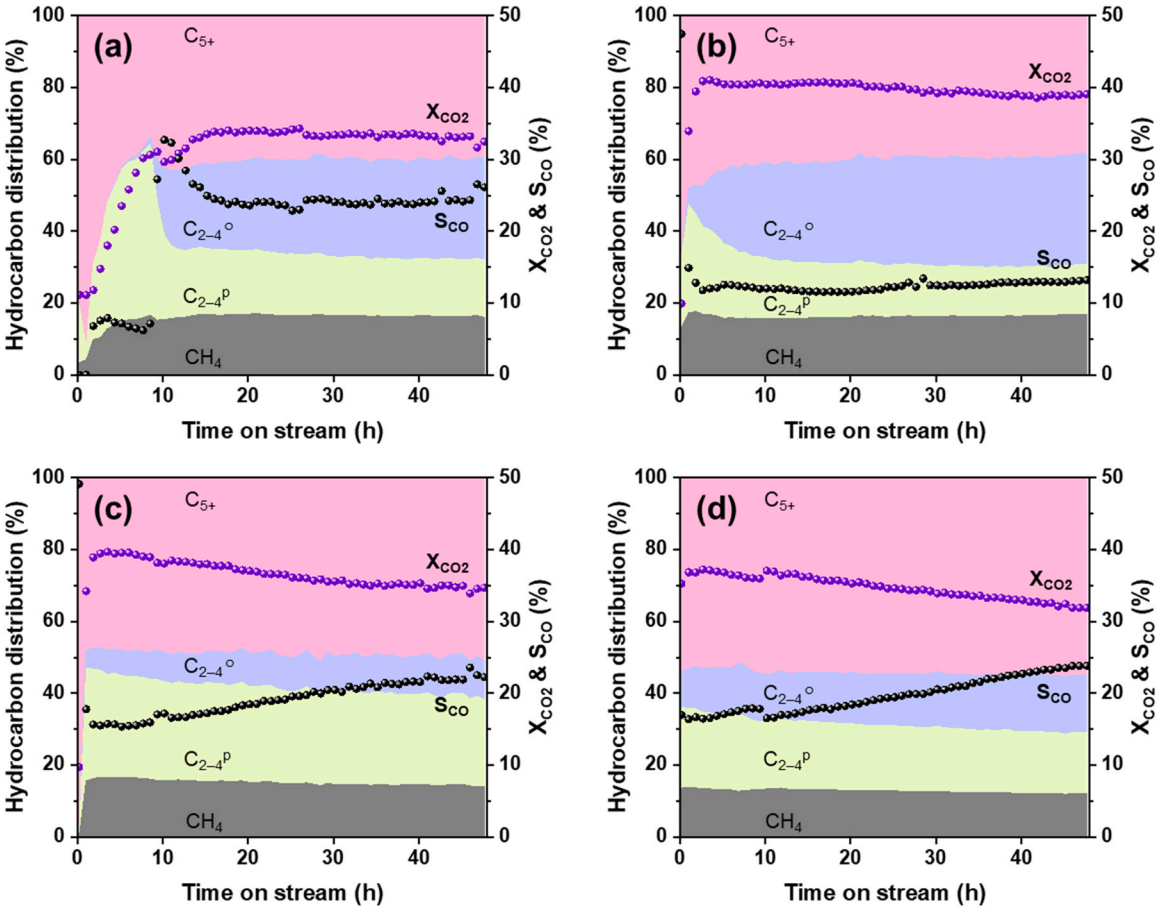

Fig. 4. Reaction profiles of the (a) PM, (b) GM, (c) DB, and (d) MB during 48 h reaction periods. The CO_2 conversion (X_{CO2}, violet dots), and CO selectivity (S_{CO}, black dots) are provided on the right y-axis. The hydrocarbon distribution is shown on the left y-axis, with CH_4 (grey), C^p_{2-4} (lime green), C^o_{2-4} (blue), and C_{5+} (pink) with filled colors to illustrate their relative contributions at different time points over the 48-hours period.

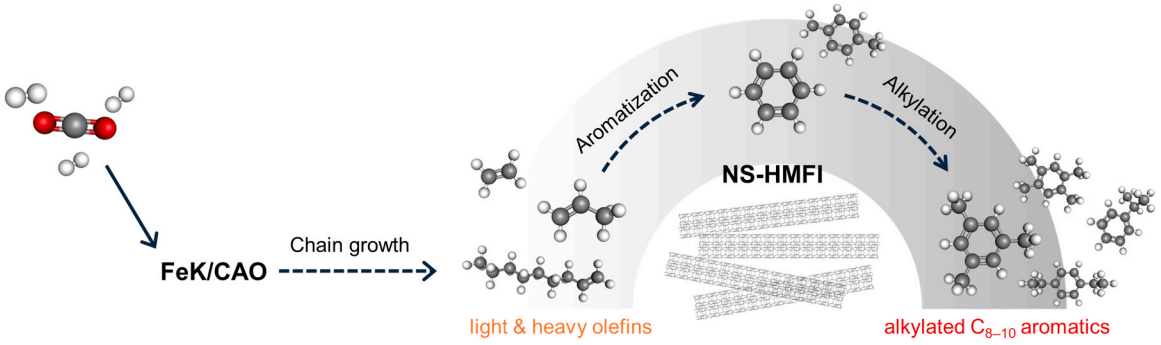

Scheme 1. Cascade reaction scheme for CO_2 hydrogenation to alkylated C_{8-10} aromatics. The scheme depicts the stepwise transformation of CO_2 and H_2 over FeK/CAO catalyst and NS-HMFI zeolite.

Table 2
Composition in aromatics represented in Fig. 3c.

Catalyst	Composition in aromatics (%)							C_{8-10}/Aro. (%)
	Benzene	Toluene	Ethylbenzene	*m/p*-xylene	*o*-xylene	C_9	C_{10}	
Physical mixture (PM)	0.3	1.9	0.9	2.4	5.0	45.7	43.9	97.7
Granule mixture (GM)	1.0	3.5	0.9	4.1	6.1	62.7	21.6	95.5
Dual-bed (DB)	0.1	1.9	0.3	4.2	11.2	64.2	18.0	98.0
Multi-bed (MB)	0.1	1.2	0.5	2.0	5.8	45.8	44.6	98.7
B-HMFI dual-bed[a]	0.0	17.8	0.0	6.9	21.6	46.5	7.2	82.2

[a] Bulk HMFI (B-HMFI) zeolite with Si/Al ratio of 40 was investigated as dual-bed catalyst system in the presence of FeK/CAO, to compare its catalytic performance with DB system consisting of FeK/CAO and NS-HMFI.

important to increase the distribution of alkylated C_{8-10} aromatic molecules than lighter aromatic molecules. Regardless of integration methods, the presence of NS-HMFI zeolite produced alkylated C_{8-10} aromatic molecules with more than 95 % selectivity among all aromatic molecules (Fig. 3c and Table 2). The major components in C_{8-10} aromatic molecules are C_9-aromatic species as analyzed by GC-MS, consisting of cumene, propylbenzene, isomers of trimethylbenzene, and isomers of methyl-ethyl-benzene, and C_{10}-aromatic species consisting of various alkylated benzene derivatives (Table S3).

To obtain aromatic molecules from CO_2 hydrogenation, it has been reported in many literatures that various catalytic components for activating multiple elementary reaction pathways are prerequisite [11,14,41,43]. In addition, construction of optimized system of multiple catalytic components is also very important [27,42,43,50]. Our catalysts consisting of FeK/CAO and NS-HMFI zeolite with various integration methods exhibited a remarkable catalytic performance that is comparable with the results reported elsewhere (Table S4). In the CO_2 hydrogenation to aromatics, it has been generally reported that either CO or methanol could be bypassed as the intermediate species depending on the catalysts and reaction conditions [40,41,43,48,50,51]. In the case of CO-intermediated route, CO_2 conversion is relatively high, but the aromatics distribution is relatively low (Table S4). In contrast, aromatics distribution is relatively high and CO_2 conversion is relatively low when methanol is intermediate species (Table S4). It is confirmed that the CO_2 conversion obtained from our catalyst system is comparable with the representative benchmark catalysts. Although aromatics distribution in all the hydrocarbon products is relatively lower than the reported works, the distribution of C_{8-10} aromatic molecules in all aromatic compounds was more than 95 % (Fig. 3c and Table 2). Accordingly, the site-time-yield of aromatics reached a remarkably high value while maintaining the high CO_2 conversion level close to 40 %, which is comparable with the highest records reported elsewhere (Fig. 3d and Table S4). The catalytic system composed of FeK/CAO and NS-HMFI zeolite realized a high yield of aromatics in CO_2 hydrogenation, with marked composition toward C_{8+} aromatic compounds (>95 %), which is comparable to or exceeds benchmark values reported in literature (Table S4).

It is well known that benzene, toluene, and *p*-xylene could diffuse in and out through 10-membered-ring micropores (ca. 0.55 nm in diameter) of MFI framework, and therefore the C_{8-10} aromatic molecules with larger kinetic diameter (>0.65 nm) could not diffuse through MFI framework [52]. Therefore, the dominant formation of C_{8-10} aromatics could be attributed to the strong acid sites located on the external surface on the mesopore wall of NS-HMFI zeolite. When we substitute NS-HMFI zeolite with conventional bulk MFI zeolite having solely microporous structure (B-HMFI), the distribution of C_{8-10} aromatic molecules in all aromatic compounds was 82.2 % which is smaller than the C_{8-10} aromatics obtained by NS-HMFI zeolite (Table 2). This could emphasize the presence of mesoporous structure having external acid sites is necessary for the formation of C_{8-10} aromatic molecules.

When we constructed MB system by locating FeK/CAO, NS-HMFI, FeK/CAO, and NS-HMFI sequentially from top to bottom layers spatially separated by quartz wool, CO_2 conversion and CO selectivity did not change significantly compared to the DB system. However, the specific hydrocarbon distribution and aromatics composition were changed (Fig. 3a–c and Tables 1–2). The zeolite amount of one layer in MB was half that in DB, which decreased accessibility of acid sites on the zeolites compared to DB. Therefore, in MB, the aromatization of olefins decelerated, resulting in slightly lower aromatics and higher distribution of olefins. Considering the distribution of aromatic compounds obtained by DB system, ratio of xylene isomers was almost halved with appreciable decrease of C_9-aromatic molecules, whereas ratio of C_{10}-aromatic molecules more than doubled in MB system (Table 2). This could be attributed to the aromatics produced in the first NS-HMFI layer underwent secondary alkylation in the second NS-HMFI layer in MB.

3.3. Mechanistic insights for CO_2 activation

Among the tested catalyst systems, the GM system exhibited the highest enhancement in CO_2 conversion compared to FeK/CAO and other catalyst systems, whereas the DB system exhibited the highest distribution increase for aromatic hydrocarbons with the lowest C_{2-4} o/p ratio (Table 1). To investigate the CO_2 activation process in GM and DB systems, we further carried out CO_2-TPD-MS (Fig. 5a–b and Table S5, also see Fig. S2 for TCD profiles). The $m/z = 44$ (CO_2) MS spectra showed that GM system had a higher CO_2 adsorption capacity than DB system (Fig. 5a), which would be associated with a higher CO_2 conversion on GM catalyst system (Fig. 3a and Table 1). In the GM system, the K in FeK/CAO migrated to the Brønsted acid site (H^+) of zeolites by ion exchange mechanism, neutralizing the acid sites and increasing the basicity throughout the GM system, resulting in greater CO_2 adsorption on the surface [43,52]. The migration of K to the zeolite surface was confirmed by STEM–EDS mapping images of the spent zeolite sample, wherein K elements were distributed throughout the nanosheet zeolite framework (Fig. S3). The increased basicity in GM promoted the dissociation of chemisorbed CO_2 to CO, thereby leading to a higher CO signal in the $m/z = 28$ (CO) MS spectra of GM system than DB system (Fig. 5b) [53]. The relative concentrations of CO and CO_2 obtained by CO_2-TPD-MS revealed a GM of 0.44, larger than the DB of 0.31, indicating the highest CO_2 activation performance of GM system (Table S5). The elevated CO_2 adsorption and dissociation in GM could promote the formation of iron carbides on FeK/CAO, thereby contributing to C_{2-4}^{o} production by raising the C/H ratio at the catalyst surface [54,55]. As shown in Fig. S4, the XRD patterns of the spent samples revealed that more iron carbides formed in GM. This would enhance CO hydrogenation, resulting in lower CO selectivity and a higher C_{2-4} o/p ratio compared to DB (Fig. 3a and Table 1).

The behavior of CO adsorption, activation, followed by hydrogenation was examined using H_2-TPSR analysis after CO pre-adsorption (Fig. 5c–d). The $m/z = 28$ (CO) MS spectra in Fig. 5c should be originated from the non-dissociative desorption of adsorbed CO*, while the evolution of $m/z = 16$ (CH_4) MS spectra in Fig. 5d should be originated from the dissociative desorption of CO* by reacting with hydrogen species. The heterolytic cleavage of the CO species into C* and O* could produce CH* with the assistance of the H species, resulting in the CH_4 formation [56,57]. For GM, CO would also be dissociated from the migrated K over the zeolites and then be hydrogenated to CH_4 by hydrogen spillover from FeK/CAO [14]. Indeed, the $m/z = 16$ to $m/z = 28$ area ratio showed that the GM was 2.62, which was greater than the DB of 2.07, indicating more direct CO dissociative activation with higher CH_4 distribution of GM than DB (Table S6). Moreover, the CH* species formed via CO dissociation in GM could also be converted into C_{2+} hydrocarbons through the C–C coupling, resulting in higher C_{2+} hydrocarbon distribution than DB [56].

4. Conclusion

In this study, we designed and systematically investigated a bifunctional catalytic system composed of FeK/CAO and NS-HMFI zeolite for CO_2 hydrogenation to value-added hydrocarbons, particularly targeting the production of C_{8-10} aromatic molecules applicable to sustainable aviation fuel (SAF) blending. The FeK/CAO catalyst alone demonstrated multifunctional catalytic behavior, enabling CO_2 conversion via RWGS, C–C coupling, and hydrogenation pathways, while favoring C_{5+} aliphatic hydrocarbons and light olefins. Integration of NS-HMFI, a nanosheet-type zeolite with hierarchical porosity, effectively promoted the formation of aromatic hydrocarbons through acid-catalyzed secondary transformations, such as oligomerization and aromatization of light olefins. By modulating the spatial proximity between the two components through four integration methods, PM, GM, DB, and MB, we disclosed the system–performance relationship. The GM system characterized by inter-granule macropores and moderate proximity achieved

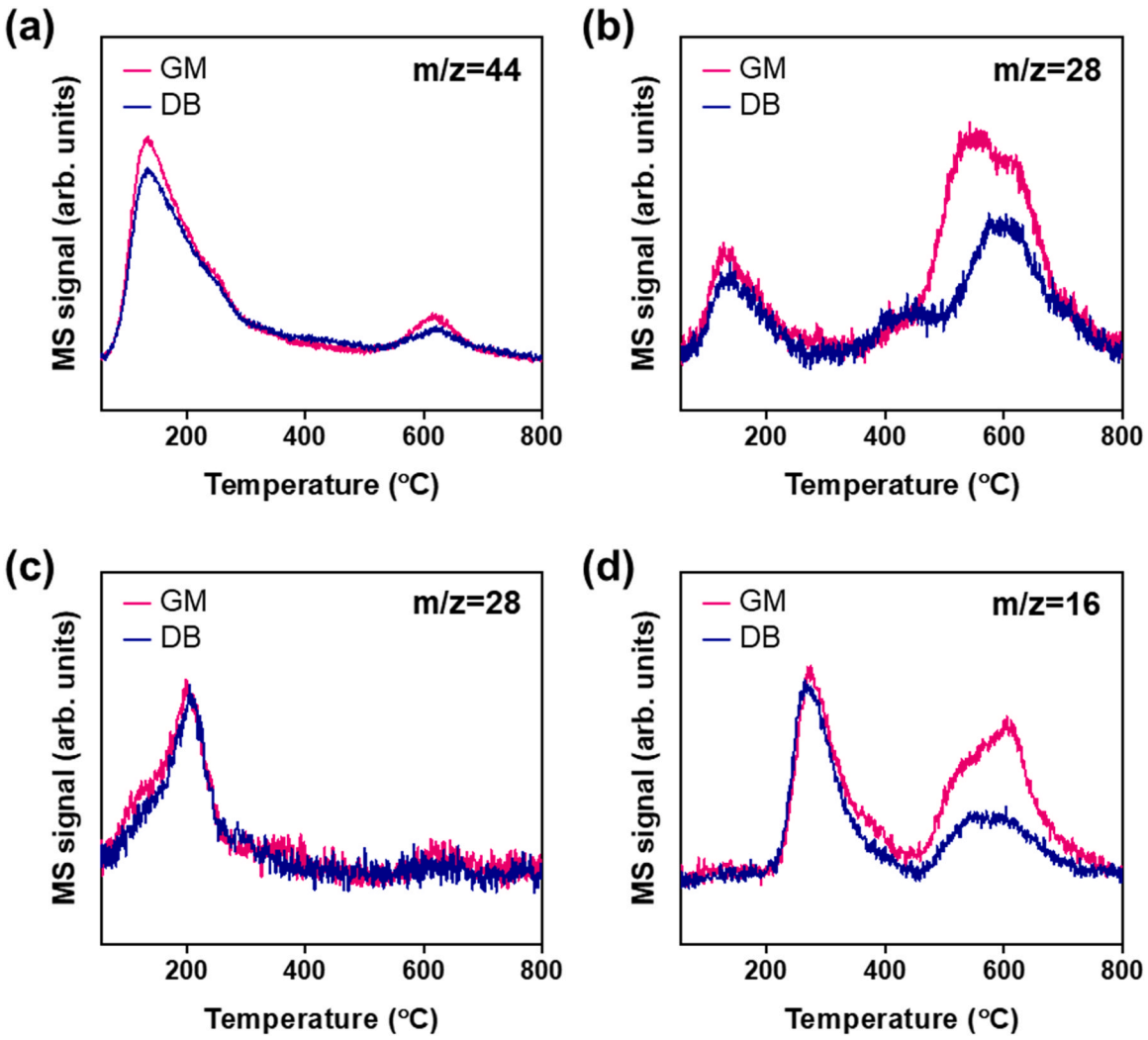

Fig. 5. (a,b) CO_2-TPD-MS profiles for GM and DB, with (a) representing $m/z = 44$ for CO_2, and (b) representing $m/z = 28$ for CO. (c,d) H_2-TPSR-MS profiles after CO adsorption for GM and DB with (c) representing $m/z = 28$ for CO and (d) representing $m/z = 16$ for CH_4.

the highest CO_2 conversion (39.2 %) and the lowest CO selectivity (13.0 %), owing to enhanced CO_2 activation facilitated by K migration and increased surface basicity. In contrast, the DB system, with minimal proximity, exhibited the highest aromatics distribution and the lowest C_{2-4} o/p ratio, highlighting the role of spatially separated acid catalysis in olefin aromatization. Importantly, across all integrated catalyst systems containing NS-HMFI, the distribution of C_{8-10} aromatic molecules exceeded 95 % among total aromatics, surpassing conventional microporous zeolites. This proves the crucial role of external acid sites on the mesoporous nanosheet zeolite in selectively producing SAF-suitable aromatics. Mechanistic investigations further confirmed the superior CO_2 and CO activation in the GM system, supported by CO_2-TPD-MS and H_2-TPSR analyses. This work offers mechanistic and structural insights into proximity-tuned bifunctional catalysis, presenting a promising strategy for direct CO_2 conversion into SAF-range aromatic hydrocarbons through rational integration of metal–acid functionalities.

CRediT authorship contribution statement

Hyeonji Yeom: Writing – review & editing, Writing – original draft, Investigation, Data curation. **Yongseok Kim:** Writing – review & editing, Writing – original draft, Investigation, Data curation. **Hanbit Jang:** Investigation, Data curation. **Jongmin Park:** Investigation, Data curation. **Seongeun Kim:** Investigation, Data curation. **Kyungsu Na:** Writing – review & editing, Writing – original draft, Supervision, Project administration, Investigation, Funding acquisition, Data curation, Conceptualization.

Declaration of Competing Interest

The authors declare that they have no known competing financial interests or personal relationships that could have appeared to influence the work reported in this paper.

Acknowledgements

This work was supported by the National Research Foundation of Korea (NRF) grant funded by the Korea government (MSIT) (RS-2024–00466475 and RS-2024–00349276), and by the Global-Learning & Academic research institution for Master's·PhD students, and Postdocs (LAMP) Program of the NRF grant funded by the Ministry of Education (RS-2024–00442775).

Appendix A. Supporting information

Supplementary data associated with this article can be found in the online version at doi:10.1016/j.cattod.2025.115574

Data availability

Supplementary material file was submitted.

References

[1] M.D. Porosoff, B. Yan, J.G. Chen, Catalytic reduction of CO_2 by H_2 for synthesis of CO, methanol and hydrocarbons: challenges and opportunities, Energy Environ. Sci. 9 (2016) 62–73, https://doi.org/10.1039/C5EE02657A.

[2] Y.A. Daza, J.N. Kuhn, CO_2 conversion by reverse water gas shift catalysis: comparison of catalysts, mechanisms and their consequences for CO_2 conversion to liquid fuels, RSC Adv. 6 (2016) 49675–49691, https://doi.org/10.1039/C6RA05414E.

[3] P. Gao, L. Zhang, S. Li, Z. Zhou, Y. Sun, Novel heterogeneous catalysts for CO_2 hydrogenation to liquid fuels, ACS Cent. Sci. 6 (2020) 1657–1670, https://doi.org/10.1021/acscentsci.0c00976.

[4] W. Tu, C. Sun, Z. Zhang, W. Liu, H.S. Malhi, W. Ma, M. Zhu, Y.-F. Han, Chemical and structural properties of na decorated Fe_5C_2-ZnO catalysts during hydrogenation of CO_2 to linear α-olefins, Appl. Catal. B Environ. 298 (2021) 120567, https://doi.org/10.1016/j.apcatb.2021.120567.

[5] K. Cheng, Y. Li, J. Kang, Q. Zhang, Y. Wang, Selectivity control by relay catalysis in CO and CO_2 hydrogenation to multicarbon compounds, Acc. Chem. Res. 57 (2024) 714–725, https://doi.org/10.1021/acs.accounts.3c00734.

[6] R. Ye, J. Ding, T.R. Reina, M.S. Duyar, H. Li, W. Luo, R. Zhang, M. Fan, G. Feng, J. Sun, J. Liu, Design of catalysts for selective CO_2 hydrogenation, Nat. Synth. 4 (2025) 288–302, https://doi.org/10.1038/s44160-025-00747-1.

[7] Z. He, M. Cui, Q. Qian, J. Zhang, H. Liu, B. Han, Synthesis of liquid fuel via direct hydrogenation of CO_2, Proc. Natl. Acad. Sci. 116 (2019) 12654–12659, https://doi.org/10.1073/pnas.1821231116.

[8] S. Ahmed, W. Yoon, H. Jo, M. Irshad, M.K. Khan, J. Kim, Structure-activity relationship and deactivation behavior of iron oxide during CO_2 hydrogenation, Chem. Eng. J. 499 (2024) 156104, https://doi.org/10.1016/j.cej.2024.156104.

[9] H. Xin, L. Lin, R. Li, D. Li, T. Song, R. Mu, Q. Fu, X. Bao, Overturning CO_2 hydrogenation selectivity with high activity via reaction-induced strong metal–support interactions, J. Am. Chem. Soc. 144 (2022) 4874–4882, https://doi.org/10.1021/jacs.1c12603.

[10] Y. Kim, S. Kwon, Y. Song, K. Na, Catalytic CO_2 hydrogenation using mesoporous bimetallic spinel oxides as active heterogeneous base catalysts with long lifetime, J. CO2 Util. 36 (2020) 145–152, https://doi.org/10.1016/j.jcou.2019.11.005.

[11] Y. Kim, Y. Song, Y. Kim, K. Na, Multifunctional long-lived catalysts for direct hydrogenative conversion of CO_2 to liquid hydrocarbons with upscaling C_{5+} productivity, J. Mater. Chem. A 10 (2022) 21862–21873, https://doi.org/10.1039/D2TA05138A.

[12] A.M. Bahmanpour, F. Héroguel, M. Kılıç, C.J. Baranowski, L. Artiglia, U. Röthlisberger, J.S. Luterbacher, O. Kröcher, Cu–Al spinel as a highly active and stable catalyst for the reverse water gas shift reaction, ACS Catal. 9 (2019) 6243–6251, https://doi.org/10.1039/D2TA05138A.

[13] H.-F. Kang, Y.-J. Liu, Y. Lu, P. Zhang, M.-X. Tang, Z.-X. Gao, H. Ge, W.-B. Fan, Exploring the sustained release catalysis of $CuAl_2O_4$ spinel for highly effective CO_2 conversion to CO, J. Catal. 432 (2024) 115427, https://doi.org/10.1016/j.jcat.2024.115427.

[14] Y. Kim, Y. Kim, H. Yeom, K. Na, Consequence of controlled hydrogen spillover on FeK/$CuAl_2O_4$ in CO_2 hydrogenation, Chem. Eng. J. 493 (2024) 152614, https://doi.org/10.1016/j.cej.2024.152614.

[15] T. Witoon, N. Kachaban, W. Donphai, P. Kidkhunthod, K. Faungnawakij, M. Chareonpanich, J. Limtrakul, Tuning of catalytic CO_2 hydrogenation by changing composition of CuO–ZnO–ZrO_2 catalysts, Energy Convers. Manag. 118 (2016) 21–31, https://doi.org/10.1016/j.enconman.2016.03.075.

[16] J. Ye, N. Dimitratos, L.M. Rossi, N. Thonemann, A.M. Beale, R. Wojcieszak, Hydrogenation of CO_2 or sustainable fuel and chemical production, Science 387 (2025) eadn9388, https://doi.org/10.1126/science.adn9388. https://www.Science.org/.

[17] R.-P. Ye, J. Ding, W. Gong, M.D. Argyle, Q. Zhong, Y. Wang, C.K. Russell, Z. Xu, A. G. Russell, Q. Li, M. Fan, Y.-G. Yao, CO_2 hydrogenation to high-value products via heterogeneous catalysis, Nat. Commun. 10 (2019) 5698, https://doi.org/10.1038/s41467-019-13638-9.

[18] K. Stangeland, H. Li, Z. Yu, CO_2 hydrogenation to methanol: the structure–activity relationships of different catalyst systems, Energy Ecol. Environ. 5 (2020) 272–285, https://doi.org/10.1007/s40974-020-00156-4.

[19] C. Qin, Y. Du, K. Wu, Y. Xu, R. Li, H. Fan, D. Xu, M. Ding, Facet-Controlled Cu-doped and K-promoted Fe_2O_3 nanosheets for efficient CO_2 hydrogenation to liquid hydrocarbons, Chem. Eng. J. 467 (2023) 143403, https://doi.org/10.1016/j.cej.2023.143403.

[20] Y. Shi, W. Gao, G. Liu, N. Tsubaki, A review of CO_2 hydrogenation to liquid fuels, ChemSusChem 18 (2025) e202402756, https://doi.org/10.1002/cssc.202402756.

[21] L. Guo, X. Gao, W. Gao, H. Wu, X. Wang, S. Sun, Y. Wei, Y. Kugue, X. Guo, J. Sun, High-yield production of liquid fuels in CO_2 hydrogenation on a zeolite-free Fe-based catalyst, Chem. Sci. 14 (2023) 171–178, https://doi.org/10.1039/D2SC05047A.

[22] D.D. Suppiah, W.M.A.W. Daud, M.R. Johan, Supported metal oxide catalysts for CO_2 Fischer–Tropsch conversion to liquid fuels—a review, Energy Fuels 35 (2021) 17261–17278, https://doi.org/10.1021/acs.energyfuels.1c02406.

[23] A.J. Barrios, D.V. Peron, A. Chakkingal, A.I. Dugulan, S. Moldovan, K. Nakouri, J. Thuriot-Roukos, R. Wojcieszak, J.W. Thybaut, M. Virginie, Efficient promoters and reaction paths in the CO_2 hydrogenation to light olefins over zirconia-supported iron catalysts, ACS Catal. 12 (2022) 3211–3225, https://doi.org/10.1021/acscatal.1c05648.

[24] Y. Guo, L. Jia, Z. Zhang, M. Gong, S. Dang, Y. Huang, X. Gao, W. Tu, Y.-F. Han, Revealing the mechanism of ce promoter in modulating product distribution of CO_2 hydrogenation over Fe-based catalysts, Chem. Eng. J. 491 (2024) 151964, https://doi.org/10.1016/j.cej.2024.151964.

[25] R.-P. Ye, J. Ding, W. Gong, M.D. Argyle, Q. Zhong, Y. Wang, C.K. Russell, Z. Xu, A. G. Russell, Q. Li, CO_2 hydrogenation to high-value products via heterogeneous catalysis, Nat. Commun. 10 (2019) 5698, https://doi.org/10.1038/s41467-019-13638-9.

[26] P. Gao, S. Li, X. Bu, S. Dang, Z. Liu, H. Wang, L. Zhong, M. Qiu, C. Yang, J. Cai, Direct conversion of CO_2 into liquid fuels with high selectivity over a bifunctional catalyst, Nat. Chem. 9 (2017) 1019–1024, https://doi.org/10.1038/nchem.2794.

[27] J. Wei, Q. Ge, R. Yao, Z. Wen, C. Fang, L. Guo, H. Xu, J. Sun, Directly converting CO_2 into a gasoline fuel, Nat. Commun. 8 (2017) 15174, https://doi.org/10.1038/ncomms15174.

[28] A. Noreen, M. Li, Y. Fu, C.C. Amoo, J. Wang, E. Maturura, C. Du, R. Yang, C. Xing, J. Sun, One-Pass hydrogenation of CO_2 to multibranched isoparaffins over bifunctional zeolite-based catalysts, ACS Catal. 10 (2020) 14186–14194, https://doi.org/10.1021/acscatal.0c03292.

[29] X. Shang, H. Zhuo, Q. Han, X. Yang, G. Hou, G. Liu, X. Su, Y. Huang, T. Zhang, Xylene synthesis through tandem CO_2 hydrogenation and toluene methylation over a composite ZnZrO zeolite catalyst, Angew. Chem. Int. Ed. 62 (2023) e202309377, https://doi.org/10.1002/anie.202309377.

[30] I. Nezam, W. Zhou, D.R. Shah, M.P. Bukhovko, M.R. Ball, G.S. Gusmão, A. J. Medford, C.W. Jones, Role of catalyst domain size in the hydrogenation of CO_2 to aromatics over $ZnZrO_x$/ZSM-5 catalysts, J. Phys. Chem. C. 127 (2023) 6356–6370.

[31] D. Weber, T. He, M. Wong, C. Moon, A. Zhang, N. Foley, N.J. Ramer, C. Zhang, Recent advances in the mitigation of the catalyst deactivation of CO_2 hydrogenation to light olefins, Catalysts 11 (2021) 1447, https://doi.org/10.1021/acs.jpcc.3c01306.

[32] J. Wei, R. Yao, Y. Han, Q. Ge, J. Sun, Towards the development of the emerging process of CO_2 heterogenous hydrogenation into high-value unsaturated heavy hydrocarbons, Chem. Soc. Rev. 50 (2021) 10764–10805, https://doi.org/10.1039/D1CS00260K.

[33] Z. Ma, M.D. Porosoff, Development of tandem catalysts for CO_2 hydrogenation to olefins, ACS Catal. 9 (2019) 2639–2656, https://doi.org/10.1021/acscatal.8b05060.

[34] Y. Wang, G. Wang, L.I. van der Wal, K. Cheng, Q. Zhang, K.P. de Jong, Y. Wang, Visualizing element migration over bifunctional metal-zeolite catalysts and its impact on catalysis, Angew. Chem. Int. Ed. 133 (2021) 17876–17884, https://doi.org/10.1002/ange.202107264.

[35] Y. Wang, L. Tan, M. Tan, P. Zhang, Y. Fang, Y. Yoneyama, G. Yang, N. Tsubaki, Rationally designing bifunctional catalysts as an efficient strategy to boost CO_2 hydrogenation producing value-added aromatics, ACS Catal. 9 (2019) 895–901, https://doi.org/10.1021/acscatal.8b01344.

[36] M. Choi, K. Na, J. Kim, Y. Sakamoto, O. Terasaki, R. Ryoo, Stable single-unit-cell nanosheets of zeolite MFI as active and long-lived catalysts, Nature 461 (2009) 246–249, https://doi.org/10.1038/nature08288.

[37] K. Na, W. Park, Y. Seo, R. Ryong, disordered assembly of MFI zeolite nanosheets with a large volume of intersheet mesopores, Chem. Mater. 23 (2011) 1273–1279, https://doi.org/10.1021/cm103245m.

[38] C. Wen, X. Xu, X. Song, L. Lu, X. Zhuang, K. Jin, Q. Jiang, X. Zhang, L. Chen, C. Wang, L. Ma, Selective CO_2 hydrogenation to light aromatics over the Cu-modified Fe-based/ZSM-5 catalyst system, Energy Fuels 37 (2023) 518–528, https://doi.org/10.1021/acs.energyfuels.2c03414.

[39] J. Holladay, Z. Abdullah, J. Heyne, Sustain. Aviat. fuel Rev. Tech. Pathw. (2020), https://doi.org/10.2172/1660415.

[40] Y. Wang, S. Kazumi, W. Gao, X. Gao, H. Li, X. Guo, Y. Yoneyama, G. Yang, N. Tsubaki, Direct conversion of CO_2 to aromatics with high yield via a modified Fischer-Tropsch synthesis pathway, Appl. Catal. B Environ. 269 (2020) 118792, https://doi.org/10.1016/j.apcatb.2020.118792.

[41] Y. Yue, J. Tian, J. Ma, S. Yang, W. Li, J. Huang, Q. Li, G. Zhan, Regulation of acidity properties of ZSM-5 and proximity between metal oxide and zeolite on bifunctional catalysts for enhanced CO_2 hydrogenation to aromatics, Appl. Catal. B Environ. 355 (2024) 124158, https://doi.org/10.1016/j.apcatb.2024.124158.

[42] X. Wang, S.Y. Jeong, H.S. Jung, D. Shen, M. Ali, F. Zafar, C.-H. Chung, J.W. Bae, Catalytic activity for direct CO_2 hydrogenation to dimethyl ether with different proximity of bifunctional Cu-ZnO-Al_2O_3 and ferrierite, Appl. Catal. B Environ. 327 (2023) 122456, https://doi.org/10.1016/j.apcatb.2023.122456.

[43] Y. Li, L. Zeng, G. Pang, X. Wei, M. Wang, K. Cheng, J. Kang, J.M. Serra, Q. Zhang, Y. Wang, Direct conversion of carbon dioxide into liquid fuels and chemicals by coupling Green hydrogen at high temperature, Appl. Catal. B Environ. 324 (2023) 122299, https://doi.org/10.1016/j.apcatb.2022.122299.

[44] V.R. Choudhary, P. Devadas, S. Banerjee, A.K. Kinage, Aromatization of dilute ethylene over Ga-modified ZSM-5 type zeolite catalysts, Microporous Mesoporous Mater. 47 (2001) 253–267, https://doi.org/10.1016/S1387-1811(01)00385-7.

[45] H. Wang, Y. Hou, W. Sun, Q. Hu, H. Xiong, T. Wang, B. Yan, W. Qian, Insight into the effects of water on the ethene to aromatics reaction with HZSM-5, ACS Catal. 10 (2020) 5288–5298, https://doi.org/10.1021/acscatal.9b05552.

[46] E.A. Uslamin, H. Saito, N. Kosinov, E. Pidko, Y. Sekine, E.J.M. Hensen, Aromatization of ethylene over zeolite-based catalysts, Catal. Sci. Technol. 10 (2020) 2774–2785, https://doi.org/10.1039/C9CY02108F.

[47] (Dd) S. Fernandes, Cd. Oliveira Veloso, C.A. Henriques, Propylene and aromatics from ethylene conversion over ZSM-5: effect of zeolite composition, Catal. Today 381 (2021) 108–117, https://doi.org/10.1016/j.cattod.2020.08.014.
[48] J. Liang, H. Liu, B. Meng, L. Guo, Z. Liu, H. Feng, H. Song, X. Jiang, C. Wang, W. Gao, X. Guo, Y. He, G. Yang, S. Yasuda, Q. Liu, T. Li, Y. Pan, C. Zeng, J. Wu, G. Liu, B. Liang, N. Tsubaki, Ternary system with sandwich configuration facilitates aromatic production from CO_2 hydrogenation, Appl. Catal. B Environ. 357 (2024) 124305, https://doi.org/10.1016/j.apcatb.2024.124305.
[49] Z. Liu, Z. Wang, X. Yang, Emission characteristics of cellulosic jet biofuel blend under laminar and turbulent combustion, Biotechnol. Biofuels Bioprod. 16 (2023) 196, https://doi.org/10.1186/s13068-023-02439-4.
[50] C. Dai, X. Zhao, B. Hu, J. Zhang, Q. Hao, H. Chen, X. Guo, X. Ma, Hydrogenation of CO_2 to aromatics over Fe–K/alkaline Al_2O_3 and P/ZSM-5 tandem catalysts, Ind. Eng. Chem. Res. 59 (2020) 19194–19202, https://doi.org/10.1021/acs.iecr.0c03598.
[51] J. Liu, C. Yang, S. Li, J. Zhang, X. Bu, H. Wang, T. Ji, J. Li, C.-R. Chang, Y. Shi, J. Liu, Z. Xu, P. Gao, Low-temperature CO_2 hydrogenation to aromatics over $ZnZrO_x$ integrated with boron-modified ZSM-5, Appl. Catal. B Environ. 377 (2025) 125523, https://doi.org/10.1016/j.apcatb.2025.125523.
[52] K. Cheng, W. Zhou, J. Kang, S. He, S. Shi, Q. Zhang, Y. Pan, W. Wen, Y. Wang, Bifunctional catalysts for one-step conversion of syngas into aromatics with excellent selectivity and stability, Chem 3 (2017) 334–347, https://doi.org/10.1016/j.chempr.2017.05.007.
[53] F. Solymosi, L. Bugyi, Effects of potassium on the chemisorption of CO_2 and CO on the Mo_2C/Mo(100) surface, Catal. Lett. 66 (2000) 227–230, https://doi.org/10.1023/A:1019092800186.
[54] N. Boreriboon, X. Jiang, C. Song, P. Prasassarakich, Higher hydrocarbons synthesis from CO_2 hydrogenation over K- and La-promoted Fe–Cu/TiO_2 catalysts, Top. Catal. 61 (2018) 1551–1562, https://doi.org/10.1007/s11244-018-1023-1.
[55] J. Jiang, C. Wen, Z. Tian, Y. Wang, Y. Zhai, L. Chen, Y. Li, Q. Liu, C. Wang, L. Ma, Manganese-promoted Fe_3O_4 microsphere for efficient conversion of CO_2 to light olefins, Ind. Eng. Chem. Res. 59 (2020) 2155–2162, https://doi.org/10.1021/acs.iecr.9b05342.
[56] X. Nie, H. Wang, M.J. Janik, Y. Chen, X. Guo, C. Song, Mechanistic insight into C–C coupling over Fe–Cu bimetallic catalysts in CO_2 hydrogenation, J. Phys. Chem. C. 121 (2017) 13164–13174, https://doi.org/10.1021/acs.jpcc.7b02228.
[57] S.-M. Hwang, S.J. Han, J.E. Min, H.-G. Park, K.-W. Jun, S.K. Kim, Mechanistic insights into cu and k promoted Fe-catalyzed production of liquid hydrocarbons via CO_2 hydrogenation, J. CO2 Util. 34 (2019) 522–532, https://doi.org/10.1016/j.jcou.2019.08.004.